Journal of Statistical Mechanics: Theory and Experiment
An IOP and SISSA journal

Quantitative analysis of numerical estimates for the permeability of porous media from lattice-Boltzmann simulations

Ariel Narváez[1,2], Thomas Zauner[2], Frank Raischel[2], Rudolf Hilfer[2,3] and Jens Harting[1,2]

[1] Department of Applied Physics, TU Eindhoven, PO Box 513, NL-5600MB Eindhoven, The Netherlands
[2] Institute for Computational Physics, University of Stuttgart, Pfaffenwaldring 27, D-70569 Stuttgart, Germany
[3] Institute for Physics, University of Mainz, D-55099 Mainz, Germany
E-mail: j.harting@tue.nl

Received 30 May 2010
Accepted 18 October 2010
Published 19 November 2010

Online at stacks.iop.org/JSTAT/2010/P11026
doi:10.1088/1742-5468/2010/11/P11026

Abstract. During the last decade, lattice-Boltzmann simulations have been improved to become an efficient tool for determining the permeability of porous media samples. However, well-known improvements of the original algorithm are often not implemented. These include, for example, multirelaxation time schemes or improved boundary conditions, as well as different possibilities to impose a pressure gradient. This paper shows that a significant difference of the calculated permeabilities can be found unless one uses a carefully selected set-up. We present a detailed discussion of possible simulation set-ups and quantitative studies of the influence of simulation parameters. We illustrate our results by applying the algorithm to a Fontainebleau sandstone and by comparing our benchmark studies to other numerical permeability measurements in the literature.

Keywords: flow in porous media, lattice Boltzmann methods

1742-5468/10/P11026+24$30.00

Contents

1. Introduction

The accurate numerical simulation of fluid flow in porous media is important in many applications ranging from hydrocarbon production and groundwater flow to catalysis and the gas diffusion layers in fuel cells [1]. Examples include the behavior of liquid oil and gas in porous rock [2], permeation of liquid in fibrous sheets such as paper [3], determining flow in underground reservoirs and the propagation of chemical contaminants in the vadose zone [4, 5], assessing the effectiveness of leaching processes [6] and optimizing filtration and sedimentation operations [7]. An important and experimentally determinable property of porous media is the permeability, which is highly sensitive to the underlying microstructure. Comparison of experimental data to numerically obtained permeabilities can improve the understanding of the influence of different microstructures and assist in the characterization of the material.

Before the 1990s the computational power available was very limited, restricting all simulations either to small length scales or low resolution of the microstructure. Shortly after its introduction lattice-Boltzmann (LB) simulations became popular [8]–[10] as an alternative to a direct numerical solution of the Stokes equation [11, 12] for simulating fluid flow in complex geometries. Historically, the LB method was developed from the lattice gas automata [10, 13]. In contrast to its predecessor, in the LB method the number of particles in each lattice direction is replaced with the ensemble average of the single-particle distribution function, and the discrete collision rule is replaced by a linear collision operator.

In the LB method all computations involve local variables so that it can be parallelized easily [12]. With the advent of more powerful computers it became possible to perform detailed simulations of flow in artificially generated geometries [3], tomographic reconstructions of sandstone samples [8, 12], [14]–[16] or fibrous sheets of paper [17].

The accuracy of LB simulations of flow in porous media depends on several conditions. These include the resolution of the discretization of the porous medium, proper boundary conditions to drive the flow and to implement the solid structure or the choice of the

J. Stat. Mech. (2010) P11026

collision kernel. Even though advanced boundary conditions and discretization methods, as well as higher-order LB kernels have been developed and are common in the literature, it is surprising to the authors that they have only found limited applications so far. In particular for commercial applications a three-dimensional implementation with 19 discrete velocities and a single relaxation time linearized collision operator is still the *de facto* standard to calculate stationary velocity fields and absolute permeabilities for porous media [18]. Here, the flow is usually driven by a uniform body force to implement a pressure gradient and solid surfaces are generated by simple bounce-back boundary conditions.

The present work is motivated by the question whether permeabilities calculated by this standard LB approach can be considered to be accurate. In particular, it is important to understand where the limits of this method are and how the accuracy can be increased. We quantify the impact of details of the implementation by studying 3D Poiseuille flow in pipes of different shape and resolution and comparing the simulation results to analytical solutions. This allows us to demonstrate how simple improvements of the simulation paradigm can lead to a substantial reduction of the error in the measured permeabilities. These include a suitable choice of the relaxation parameter τ and the application of the multirelaxation time method in order to ascertain a minimal unphysical influence of the fluid viscosity on the permeability. Further, a correct implementation of the body force to drive the flow together with suitable in- and outflow boundaries is mandatory to avoid artifacts in the steady state velocity field. Finally, the small compressibility of the LB fluid requires a proper determination of the pressure gradient in the system. If these details are taken care of, it is shown that the LB method is well suited for accurate permeability calculations of stochastic porous media by applying it to discretized micro-computer-tomography (μ-CT) data of a Fontainebleau sandstone.

2. Simulation method

The Boltzmann equation

$$\frac{\partial}{\partial t} f(\mathbf{x}, \mathbf{c}, t) + \mathbf{c} \cdot \nabla f(\mathbf{x}, \mathbf{c}, t) = \Omega(f(\mathbf{x}, \mathbf{c}, t)) \tag{1}$$

describes the evolution of the single-particle probability density $f(\mathbf{x}, \mathbf{c}, t)$, where $\mathbf{x} \in \mathbb{R}^3$ is the position vector, $\mathbf{c} \in \mathbb{R}^3$ is the velocity vector, $t \in \mathbb{R}$ is the time and $\Omega(f(\mathbf{x}, \mathbf{c}, t))$ is the collision operator. While discretizations on unstructured grids exists [19, 20], they are not widely used and typically the position $\mathbf{x}$ is discretized on a structured cubic lattice, with lattice constant Δx. The time is discretized using a time step Δt and the velocities are discretized into a finite set of vectors $\mathbf{c}_i$ with $i = 1, \ldots, N$, called lattice velocities, where the finite integer N varies between implementations. In this work we exclusively use the so-called D3Q19 lattice, where $N = 19$ velocities are used in a three-dimensional domain [21]. A cubic lattice with basis $\mathbf{e}_k \in \mathbb{R}^3$, $k = 1, 2, 3$ is embedded into $\mathbb{R}^3$ using the coordinate function $\mathbf{g} : \mathbb{N}^3 \mapsto \mathbb{R}^3$ to map the lattice nodes $\boldsymbol{\ell} \in \mathbb{N}^3$ to position vectors $\mathbf{g}(\boldsymbol{\ell}) \in \mathbb{R}^3$. The computational domain is a rectangular parallelepiped denoted as

$$\mathcal{L} = \{\boldsymbol{\ell} \in \mathbb{N}^3 : 1 \leq \ell_k \leq L_k;\ k = 1, 2, 3\}, \tag{2}$$

where $L_k \in \mathbb{N}^3$ are its dimensionless side lengths. See figure 1 for a visualization. Physical quantities w such as pressure or density on the lattice are abbreviated as $w(\boldsymbol{\ell}) = w(\mathbf{g}(\boldsymbol{\ell}))$.

J. Stat. Mech. (2010) P11026

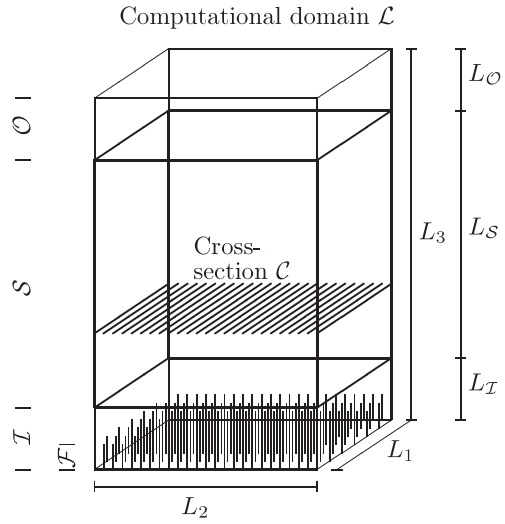

Figure 1. The computational domain $\mathcal{L}$. The (porous) sample is $\mathcal{S}$ and the fluid is accelerated in the acceleration zone $\mathcal{F}$. Two fluid chambers $\mathcal{I}$ and $\mathcal{O}$ are used to avoid artifacts.

We introduce the vector notation $\mathbf{f}(\boldsymbol{\ell}, t) = (f_1(\boldsymbol{\ell}, t), \ldots, f_N(\boldsymbol{\ell}, t))$, where the components are the probabilities calculated as

$$f_i(\boldsymbol{\ell}, t) = \int_{\mathbb{W}(\boldsymbol{\ell})} \int_{\mathbb{B}(i)} f(\mathbf{x}, \mathbf{c}, t)\, \mathrm{d}\mathbf{c}\, \mathrm{d}\mathbf{x}. \tag{3}$$

Here, $\mathbb{W}(\boldsymbol{\ell}) \subset \mathbb{R}^3$ is the finite volume associated with the point $\mathbf{g}(\boldsymbol{\ell})$ and $\mathbb{B}(i) \subset \mathbb{R}^3$ is the volume in velocity space given by lattice velocity $\mathbf{c}_i$. The macroscopic density $\rho(\boldsymbol{\ell}, t)$ and velocity $\mathbf{v}(\boldsymbol{\ell}, t)$ are obtained from $f_i(\boldsymbol{\ell}, t)$ as

$$\rho(\boldsymbol{\ell}, t) = \rho^\circ \sum_{i=1}^{N} f_i(\boldsymbol{\ell}, t), \tag{4}$$

$$\mathbf{v}(\boldsymbol{\ell}, t) = \sum_{i=1}^{N} f_i(\boldsymbol{\ell}, t)\, \mathbf{c}_i \Big/ \sum_{i=1}^{N} f_i(\boldsymbol{\ell}, t), \tag{5}$$

where ρ° is a reference density. The pressure is given by

$$p(\boldsymbol{\ell}, t) = c_\mathrm{s}^2\, \rho(\boldsymbol{\ell}, t), \tag{6}$$

with the speed of sound [10, 13]

$$c_\mathrm{s} = \frac{1}{\sqrt{3}} \left(\frac{\Delta x}{\Delta t} \right). \tag{7}$$

Discretization of equation (1) provides the basic system of difference equations in the LB method

$$f_i(\boldsymbol{\ell} + \Delta\boldsymbol{\ell}_i, t + \Delta t) - f_i(\boldsymbol{\ell}, t) = \Delta t\, \Omega_i(\boldsymbol{\ell}, t), \tag{8}$$

with $\Delta\boldsymbol{\ell}_i = \mathbf{c}_i \Delta t / \Delta x$ and the initial condition $f_i(\boldsymbol{\ell}, 0) = 1/N$ (for $t = 0$). The generally

nonlinear collision operator is approximated using the linearization

$$\Omega_i(\boldsymbol{\ell}, t) = \sum_{j=1}^{N} S_{ij}(f_j(\boldsymbol{\ell}, t) - f_j^{\mathrm{eq}}(\boldsymbol{\ell}, t)), \tag{9}$$

around a local equilibrium probability function $\mathbf{f}^{\mathrm{eq}}(\boldsymbol{\ell}, t) = (f_1^{\mathrm{eq}}(\boldsymbol{\ell}, t), \ldots, f_N^{\mathrm{eq}}(\boldsymbol{\ell}, t))$, with an $N \times N$ collision matrix $\mathbf{S}$ [22, 23].

The simplest approach to define the collision matrix uses a single relaxation time with time constant τ,

$$S_{ij} = -\frac{1}{\tau}\,\delta_{ij}, \tag{10}$$

where δ_{ij} is the Kronecker delta. This single relaxation time (LB-BGK) scheme is named after the original work of Bhatnagar, Gross and Krook [24, 25]. Within the LB-BGK method, $\mathbf{f}^{\mathrm{eq}}(\boldsymbol{\ell}, t)$ is approximated by a second-order Taylor expansion of the Maxwell distribution [26]:

$$f_i^{\mathrm{eq}}(\boldsymbol{\ell}, t) = \frac{\rho\omega_{\mathbf{c}_i}}{\rho^{\circ}}\left(1 + \frac{\mathbf{v}^* \cdot \mathbf{c}_i}{c_{\mathrm{s}}^2} + \frac{(\mathbf{v}^* \cdot \mathbf{c}_i)^2}{2c_{\mathrm{s}}^4} - \frac{\mathbf{v}^* \cdot \mathbf{v}^*}{2c_{\mathrm{s}}^2}\right). \tag{11}$$

If external forces are absent, the equilibrium velocity is defined as $\mathbf{v}^*(\boldsymbol{\ell}, t) = \mathbf{v}(\boldsymbol{\ell}, t)$ from equation (5). As explained further below, $\mathbf{v}^*(\boldsymbol{\ell}, t)$ and $\mathbf{v}(\boldsymbol{\ell}, t)$ may differ from equation (5) if an external acceleration is present. The numbers $\omega_{\mathbf{c}_i}$ are called lattice weights and differ with lattice type, number of space dimensions and number of discrete velocities N. See [10] for a comprehensive overview on different lattices.

An alternative approach to specify the collision matrix is the multirelaxation time (MRT) method. Here, a linear transformation $\mathbf{M}$ is chosen such that the moments

$$m_i(\boldsymbol{\ell}, t) = \sum_{j}^{N} M_{ij}\, f_j(\boldsymbol{\ell}, t) \tag{12}$$

represent hydrodynamic modes of the problem. We use the definitions given in [27], where $m_1(\boldsymbol{\ell}, t)$ is the density defined in equation (4), $m_2(\boldsymbol{\ell}, t)$ represents the energy, $m_i(\boldsymbol{\ell}, t)$ with $i = 4, 6, 8$ the momentum flux and $m_i(\boldsymbol{\ell}, t)$, with $i = 10, 12, 14, 15, 16$ are components of the symmetric traceless stress tensor. Introducing the moment vector $\mathbf{m}(\boldsymbol{\ell}, t) = (m_1(\boldsymbol{\ell}, t), \ldots, m_N(\boldsymbol{\ell}, t))$, $\boldsymbol{\Omega}(\boldsymbol{\ell}, t) = (\Omega_1(\boldsymbol{\ell}, t), \ldots, \Omega_N(\boldsymbol{\ell}, t))$, a diagonal matrix $\check{S}_{ij} = \check{s}_i\,\delta_{ij}$, and the equilibrium moment vector $\mathbf{m}^{\mathrm{eq}}(\boldsymbol{\ell}, t) = (m_1^{\mathrm{eq}}(\boldsymbol{\ell}, t), \ldots, m_N^{\mathrm{eq}}(\boldsymbol{\ell}, t))$, we obtain

$$\boldsymbol{\Omega}(\boldsymbol{\ell}, t) = -\mathbf{M}^{-1} \cdot \check{\mathbf{S}} \cdot (\mathbf{m}(\boldsymbol{\ell}, t) - \mathbf{m}^{\mathrm{eq}}(\boldsymbol{\ell}, t))\,. \tag{13}$$

During the collision step the density and the momentum flux are conserved so that $m_1^{\mathrm{eq}}(\boldsymbol{\ell}, t) = m_1(\boldsymbol{\ell}, t)$ and $m_i(\boldsymbol{\ell}, t) = m_i^{\mathrm{eq}}(\boldsymbol{\ell}, t)$ with $i = 2, 4, 6$. The non-conserved equilibrium moments $m_i^{\mathrm{eq}}(\boldsymbol{\ell}, t)$, $i \neq 1, 2, 4, 6$, are assumed to be functions of these conserved moments and explicitly given, for example, in [27]. The diagonal element $\tau_i = 1/\check{s}_i$ in the collision matrix is the relaxation time moment $m_i(\boldsymbol{\ell}, t)$. One has $\check{s}_1 = \check{s}_4 = \check{s}_6 = \check{s}_8 = 0$, because the corresponding moments are conserved, $\check{s}_2 = 1/\tau_{\mathrm{bulk}}$ describes the relaxation of the energy and $\check{s}_{10} = \check{s}_{12} = \check{s}_{14} = \check{s}_{15} = \check{s}_{16} = 1/\tau$ the relaxation

J. Stat. Mech. (2010) P11026

of the stress tensor components. The remaining diagonal elements of $\check{\mathbf{S}}$ are chosen as

$$\check{\mathbf{S}} = \mathrm{diag}(0, 1/\tau_{\mathrm{bulk}}, 1.4, 0, 1.2, 0, 1.2, 0, 1.2, 1/\tau, \\ 1.4, 1/\tau, 1.4, 1/\tau, 1/\tau, 1/\tau, 1.98, 1.98, 1.98), \tag{14}$$

to optimize the algorithm performance [27, 28]. Because two parameters τ and τ_{bulk} remain free, the multirelaxation time method reduces to a 'two relaxation time' (TRT) method. An alternative TRT implementation can be found in [29, 30].

To apply the LB method to viscous flow in porous media it is necessary to establish its relations with hydrodynamics. The Chapman–Enskog procedure shows that density, velocity and pressure fulfill the Navier–Stokes equations without external forces, with a kinematic viscosity [26], [31]–[34]

$$\nu(\tau, \Delta t) = c_{\mathrm{s}}^2 \Delta t \left(\frac{\tau}{\Delta t} - \frac{1}{2} \right). \tag{15}$$

Combining equations (15) and (7) gives

$$\frac{\tau}{\Delta t} = \frac{1}{2} + \frac{\sqrt{3}\,\nu}{c_{\mathrm{s}}\,\Delta x} = \frac{1}{2} + 3\frac{\nu\,\Delta t}{(\Delta x)^2}. \tag{16}$$

Because $\nu \geq 0$, $\Delta x > 0$ and $\Delta t > 0$, it follows that $\tau/\Delta t \geq 1/2$.

A typical value for the pore diameter in sandstone is $a \approx 10^{-5}$ m, and for water the kinematic viscosity and speed of sound are $\nu \approx 10^{-6}$ m^2 s^{-1} and $c_{\mathrm{s}} \approx 10^3$ m s^{-1}, respectively. With typical velocities of order $v \approx 10^{-4}$ m s^{-1} the Reynolds number is $Re = v\,a/\nu \approx 10^{-3}$. Discretizing with $\Delta x = 10^{-6}$ m gives then $\tau/\Delta t = 0.5017$. Because for $\tau/\Delta t \approx 1/2$ the LB method is known to be unstable, a direct simulation of water flow in porous media with these parameters is not feasible. To overcome this impasse, one might impose $\tau/\Delta t = 1$ and simultaneously fix ν and c_{s} as fluid parameters. The discretization then is $\Delta t \approx 10^{-12}$ s and $\Delta x \approx 10^{-9}$ m. Again, a simulation with these parameters is not possible because a typical pore with diameter $a \approx 10^{-5}$ m would have to be represented by 10^4 nodes, exceeding realistic memory capacities. Another way to circumvent these problems is to appeal to hydrodynamic similarity for stationary flows. The simulations in this paper are performed with fluid parameters that represent a pseudofluid with the same viscosity as water, but $c_{\mathrm{s}} = 1$ m s^{-1} as the speed of sound. The discretization then is $\Delta x = 10^{-6}$ m and $\Delta t = 10^{-6}$ s. A pore of diameter a is then represented by 10 nodes and a cubic sample with side-length 10^{-3} m requires 1000^3 nodes, a manageable system size on parallel computers. An external force, as discussed next, drives the flow such that the velocities are of order 10^{-3} m s^{-1}. The Mach and Reynolds numbers in the simulations are $Ma \approx 10^{-3}$ and $Re \approx 10^{-3}$, characterizing a laminar subsonic flow. As long as $Ma \ll 1$ and hydrodynamic similarity remains valid, we do not expect that the parameters of the pseudofluid will change the permeability estimate.

An external acceleration $\mathbf{b}(\boldsymbol{\ell}, t)$ acting on the fluid is implemented by adding two modifications. First, a forcing term written as a power series in the velocity [23]

$$\varphi_i(\boldsymbol{\ell}, t) = \Delta t \frac{\rho\,\omega_{\mathbf{c}_i}}{\rho^\circ} \left(h_0 + \frac{\mathbf{h}_1 \cdot \mathbf{c}_i}{c_{\mathrm{s}}^2} + \frac{\mathbf{h}_2 : (\mathbf{c}_i\mathbf{c}_i - c_{\mathrm{s}}^2\mathbf{I})}{2c_{\mathrm{s}}^4} \right), \tag{17}$$

is added to the right-hand side of equation (8). Second, equation (5) for the equilibrium velocity $\mathbf{v}^*$ in equation (11) needs to be modified. The parameters of order 0, 1 and 2

J. Stat. Mech. (2010) P11026

in the expansion are h_0, $\mathbf{h}_1$ and $\mathbf{h}_2$. The definition of the velocities $\mathbf{v}^*(\boldsymbol{\ell}, t)$ and $\mathbf{v}(\boldsymbol{\ell}, t)$ differ with the method used. We present four possible implementations which all assume $h_0 = 0$, since otherwise a source term in the mass balance would have to be taken into account. The sums in this paragraph run from $i = 1, \ldots, N$ and the quantities $\mathbf{h}_1$, $\mathbf{h}_2$, f_i, $\mathbf{v}$, $\mathbf{v}^*$ and $\mathbf{b}$ are functions of $\boldsymbol{\ell}$ and t unless specified otherwise.

The first method to implement a body force is referred to as METHOD A in the remainder of this paper. It uses

$$\mathbf{h}_1 = \left(1 - \frac{\Delta t}{2\tau}\right)\mathbf{b}, \qquad \mathbf{h}_2 = \left(1 - \frac{\Delta t}{2\tau}\right)(\mathbf{v}^*\mathbf{b} + \mathbf{b}\mathbf{v}^*), \tag{18}$$

and a modified definition of $\mathbf{v}^*$ and $\mathbf{v}$ which causes the influence of temporal and spatial derivatives of $\mathbf{b}$ on the density and momentum changes to vanish. For this method one obtains $\mathbf{v}^* = \mathbf{v}$, with

$$\mathbf{v} = \left(\sum f_i\,\mathbf{c}_i \Big/ \sum f_i\right) + \Delta t\,\mathbf{b}/2 \tag{19}$$

instead of equation (5). A multiscale expansion in time of the resulting discrete LB equation yields that the macroscopic density ρ and velocity $\mathbf{v}$ recover the Navier–Stokes equations with an external body force term [35]. The forcing is applied in two steps during every time step Δt, one half within the collision step by the definition of $\mathbf{v}^*$ and the second half within the streaming step by the term φ_i. In the case of LB-MRT the part which is applied during the collision step is added to the modes $m_i(\boldsymbol{\ell}, t)$ with $i = 4, 6, 8$, which represent the momentum flux.

The second method (METHOD B) is defined by setting

$$\mathbf{h}_1 = \mathbf{b}, \qquad \mathbf{h}_2 = \mathbf{0}, \tag{20}$$

so that $\varphi_i(\boldsymbol{\ell})$ does not depend on $\mathbf{v}^*(\boldsymbol{\ell}, t)$. The full acceleration is applied only within the streaming step through the term $\varphi_i(\boldsymbol{\ell})$. One sets

$$\mathbf{v}^* = \sum f_i\,\mathbf{c}_i \Big/ \sum f_i, \tag{21}$$

and the macroscopic velocity $\mathbf{v}$ defined as in equation (19). This simplification is useful because it reduces the computational effort, but it is restricted to stationary flows. In our simulations $\mathbf{b}(\boldsymbol{\ell})$ is time-independent and we are mainly interested in the permeability and stationary flows so that we have adopted METHOD B in our simulations below. In METHOD B the macroscopic fields fulfill mass balance, but some additional unphysical terms appear in the momentum balance [35]. Here we assume that all these additional terms are negligible or vanish for stationary flows, because we expect that all spatial gradients are sufficiently small.

METHOD C is intended for constant $\mathbf{b}$ and uses the same parameters $\mathbf{h}_1$ and $\mathbf{h}_2$ as METHOD B [36]. However, the macroscopic velocity $\mathbf{v} = \mathbf{v}^*$ is calculated as in equation (21). This recovers momentum balance, because unphysical terms either vanish or are negligible, but it does not recover mass balance, which in this case is

$$\frac{\partial \rho}{\partial t} + \nabla \cdot (\rho \mathbf{v}) = -\frac{\Delta t}{2} \nabla \cdot (\rho \mathbf{b}). \tag{22}$$

The reason is an inaccurate calculation of the macroscopic velocity $\mathbf{v}(\boldsymbol{\ell}, t)$ [35]. The impact of this issue on the simulation results is shown in section 5.

J. Stat. Mech. (2010) P11026

METHOD D suggests we incorporate the acceleration not by using the forcing term, but by adding the term $\tau\mathbf{b}(\boldsymbol{\ell},t)$ to the equilibrium velocity $\mathbf{v}^*(\boldsymbol{\ell},t)$. The macroscopic velocity $\mathbf{v}(\boldsymbol{\ell},t)$ remains calculated by equation (5) [37]. This is equivalent to using the forcing term with

$$\mathbf{h}_1 = \mathbf{b}, \qquad \mathbf{h}_2 = \tau\mathbf{b}\mathbf{b} + \mathbf{b}\mathbf{v}^* + \mathbf{v}^*\mathbf{b}, \tag{23}$$

and $\mathbf{v} = \mathbf{v}^*$ given by equation (21). This implementation leads to the same drawback in the mass balance equation as in METHOD C.

The most common boundary conditions (BC) used jointly within LB implementations are periodic (PBC) and no-slip BC. When using PBC, fluid that leaves the domain, i.e. the term $\boldsymbol{\ell} + \Delta\boldsymbol{\ell}_i$ in equation (8), exceeds the computational domain size and enters the domain from the other side. The no-slip BC, also called the simple bounce-back rule (SBB), approximates vanishing velocities at solid surfaces [13]. If the lattice point $\boldsymbol{\ell}+\Delta\boldsymbol{\ell}_i$ in equation (8) represents a solid node, the discrete LB equation is rewritten as

$$f_i^*(\boldsymbol{\ell}, t+\Delta t) - f_i(\boldsymbol{\ell}, t) = \Delta t\, \Omega_i(\boldsymbol{\ell}, t), \tag{24}$$

where the probability function f_i^* is associated with $\mathbf{c}_i^*$, where $\mathbf{c}_i^* = -\mathbf{c}_i$ is the probability function in the opposite direction to f_i. Midplane BC [37] improve the SBB eliminating the zig-zag profile when plotting the mass flow q versus ℓ_3, but yield the same mass flow Q, see equations (27) and (28) for their definition, respectively. The SBB scheme depends on viscosity and relaxation time τ, especially in under-relaxed simulations (large values of τ) [36]. The numerically exact position of the fluid–solid interface changes slightly for different τ which can pose a severe problem when simulating flow within porous media, where some channels might only be a few lattice units wide. The permeability κ, being a material constant of the porous medium alone, becomes dependent on the fluid viscosity. As demonstrated below within the LB-MRT method this κ–τ correlation is significantly smaller than within LB-BGK [27, 38]. Recently, further improvements for no-slip BC have been discussed [33]. Most of these implementations use a spatial interpolation, for example, linearly and quadratic interpolated bounce-back [39, 40] or multireflection [41]. To calculate boundary effects these methods use multiple nodes in the vicinity of the surface. For this reason these schemes are unsuitable in porous media where some pore throats might be represented by two or three nodes only. Consequently, we use midplane BC as well as PBC for our simulations.

To drive the flow on-site pressure or flux BC [42, 43] may be used. Using them it is possible to exactly set the ideal gas pressure (or density, see equation (6)) or flux on a specific node. Thus, creating a pressure gradient by fixing either the pressure or the mass flux at the inlet and outlet nodes are feasible alternatives.

3. Simulation set-up

The computational domain (see figure 1) $\mathcal{L}$ is composed of three zones: the sample $\mathcal{S}$ describing the geometry and two chambers $\mathcal{I}$ (inlet) and $\mathcal{O}$ (outlet), before and after the sample, containing fluid reservoirs. The notation

$$\mathcal{C}(a) := \{\boldsymbol{\ell} \in \mathcal{L} : \ell_3 = a\} \tag{25}$$

denotes a cross section, where $\mathcal{C}(L_\mathcal{I})$, $\mathcal{C}(L_\mathcal{I}+1)$, $\mathcal{C}(L_3 - L_\mathcal{O})$ and $\mathcal{C}(L_3 - L_\mathcal{O}+1)$ represent the cross sections right before the sample ($\mathcal{C}(L_\mathcal{I}) \in \mathcal{I}$), the first ($\mathcal{C}(L_\mathcal{I}+1) \in \mathcal{S}$) and

J. Stat. Mech. (2010) P11026

last ($\mathcal{C}(L_3 - L_\mathcal{O}) \in \mathcal{S}$) cross section within the sample, and the cross section right after the sample ($\mathcal{C}(L_3 - L_\mathcal{O} + 1) \in \mathcal{O}$), respectively. Every lattice point (node) in $\mathcal{L}$ is either part of the matrix, denoted $\mathcal{M}$, or part of the fluid, denoted $\mathcal{P}$, so that $\mathcal{M} \cup \mathcal{P} = \mathcal{L}$ and $\mathcal{M} \cap \mathcal{P} = \emptyset$.

Results are presented in the dimensionless quantities

$$\begin{aligned}
&\hat{\mathbf{x}} = \mathbf{x}/\Delta x, \qquad \hat{t} = t/\Delta t, \qquad \hat{\rho} = \rho/\rho^\circ, \qquad \hat{p} = p/(3{c_\mathrm{s}}^2\rho^\circ),\\
&\hat{\mathbf{v}} = \mathbf{v}\Delta t/\Delta x, \qquad \hat{\tau} = \tau/\Delta t, \qquad \hat{\tau}_\mathrm{bulk} = \tau_\mathrm{bulk}/\Delta t,\\
&\hat{\kappa} = \kappa/(\Delta x)^2, \qquad \hat{b} = b\,(\Delta t)^2/\Delta x, \qquad \hat{q} = q\,\Delta t/(\rho^\circ\,(\Delta x)^3),
\end{aligned}$$

where the discretization parameters Δx and Δt are chosen according to the analysis presented in section 2. Unless otherwise noted, the relaxation time is $\hat{\tau} = 0.857$ and for LB-MRT simulations $\hat{\tau}_\mathrm{bulk} = 1.0$ is used. Generally, results from LB simulations are labeled with the superscript '$^\mathrm{LB}$', e.g. the density ρ^LB. If the results refer to a specific implementation (BGK or MRT) they are labeled accordingly, e.g. ρ^BGK or ρ^MRT.

The fluid is driven using MODEL B. The acceleration $\mathbf{b} = b\,\mathbf{e}_3$ is not applied throughout the whole domain but only within the acceleration zone $\mathcal{F} \subset \mathcal{I}$. An acceleration of $\hat{b} = 10^{-6}$ is used for all simulations.

The average for a physical quantity w is

$$\langle w \rangle_\mathcal{V} = \frac{1}{|\mathcal{V}|} \sum_{\boldsymbol{\ell} \in \mathcal{V}} w(\boldsymbol{\ell}), \tag{26}$$

with the domain $\mathcal{V} \in \{\mathcal{L}, \mathcal{S}, \mathcal{P}, \mathcal{I}, \mathcal{O}, \mathcal{F}, \mathcal{C}(a)\}$ and $|\mathcal{V}|$ the number of nodes in that domain. The mass flow q through a cross section $\mathcal{C}(a)$ is given by

$$q(a) = \sum_{\boldsymbol{\ell} \in \mathcal{C}(a) \cap \mathcal{P}} \rho(\boldsymbol{\ell})\, v_3(\boldsymbol{\ell}) (\Delta x)^2, \tag{27}$$

with $\rho(\boldsymbol{\ell}) v_3(\boldsymbol{\ell})$ being the momentum component in the direction of the flow. The mass flow through the whole domain is

$$Q = \frac{1}{L_3} \sum_{\ell_3 = 1}^{L_3} q(\ell_3). \tag{28}$$

4. Calibration

To calibrate the simulation we simulate Poiseuille flow in pipes with quadratic cross section. The simulation parameters are defined by

$$\begin{aligned}
&\mathbf{g}(\boldsymbol{\ell}) = \left(\ell_1 - \frac{L_1 + 1}{2}\right) \Delta x \mathbf{e}_1 + \left(\ell_2 - \frac{L_2 + 1}{2}\right) \Delta x \mathbf{e}_2 + \left(\ell_3 - \frac{1}{2}\right) \Delta x \mathbf{e}_3,\\
&\mathcal{S} = \{\boldsymbol{\ell} \in \mathcal{L} : 2 \le \ell_1 \le L_1 - 1,\ 2 \le \ell_2 \le L_2 - 1,\ 4 \le \ell_3 \le L_3 - L_\mathcal{O}\},\\
&\mathcal{I} = \{\boldsymbol{\ell} \in \mathcal{L} : \ell_3 \le L_\mathcal{I}\}, \qquad \mathcal{O} = \{\boldsymbol{\ell} \in \mathcal{L} : L_3 - L_\mathcal{O} \le \ell_3 \le L_3\},\\
&\mathcal{F} = \{\boldsymbol{\ell} \in \mathcal{L} : \ell_3 \le 2\}
\end{aligned} \tag{29}$$

where $L_\mathcal{I} = 3, L_\mathcal{S} = L_3 - 6$ and $L_\mathcal{O} = 3$. The system dimensions are $L_1 = L_2 = \hat{B} + 2$, $L_3 = 4\hat{B}$, with $B/\Delta x = \hat{B} \in \{4, 8, 16, 32, 64\}$ the channel width.

J. Stat. Mech. (2010) P11026

According to [44] the analytical solution for the velocity component in the flow direction in a pipe with quadratic cross section is

$$\begin{aligned} v^{\mathrm{TH}}(x_1, x_2) &= \lim_{M\to\infty} v(x_1, x_2, M) \\ v(x_1, x_2, M) &= -\frac{(\nabla p)_3}{2\eta}\left(\frac{B^2}{4} - {x_2}^2 - \frac{8B^2}{\pi^3}\sum_{n=0}^{M} C_n\right), \\ C_n &= (-1)^n \frac{\cosh\left(\frac{(2n+1)\pi}{B}x_1\right)\cos\left(\frac{(2n+1)\pi}{B}x_2\right)}{(2n+1)^3\cosh\left(\frac{(2n+1)\pi}{2}\right)} \end{aligned} \tag{30}$$

where $x_1 \in [-B/2, B/2]$ and $x_2 \in [-B/2, B/2]$. The Cartesian coordinates x_1 and x_2 have their origin in the center of the pipe. $(\nabla p)_3$ is the pressure gradient in the flow direction and η is the dynamic viscosity. The expression $v(x_1, x_2, M)$ is asymmetric in x_1 and x_2. Contrary to the no-slip condition the velocities $v(B/2, x_2, M)$ are not zero for finite M. To estimate the truncation error we define

$$\tilde{v}(x, M) = \frac{2\eta}{(\nabla p)_3 B^2}\, v(B/2, x, M), \qquad x \in [-B/2, B/2], \tag{31}$$

and

$$\|\tilde{v}_{\mathrm{wall}}(M)\|_2 := \sqrt{\frac{1}{B}\int_{-B/2}^{B/2} |\tilde{v}(x, M)|^2 \,\mathrm{d}x}, \tag{32}$$

with $\tilde{v}(x, M)$ being the normalized velocities on the wall calculated from equation (31). $\|\tilde{v}_{\mathrm{wall}}(M)\|_2$ quantifies the truncation error at finite M. Requiring that the truncation error $\|\tilde{v}_{\mathrm{wall}}(M)\|_2$ is at least three to four decades smaller than the velocities in the corners, for example $\tilde{v}(\mathbf{g}(1, 1, L_3/2)_1, \mathbf{g}(1, 1, L_3/2)_2, M)$ or any other such corner velocity, yields $M \approx 50$. For all further comparisons with LB simulations we use $M = 200$. If M is chosen too small, a meaningful comparison of the simulation results with the analytical solution is not possible because of the inaccuracies in the numerical evaluation of the analytical solution itself.

Equation (30) is the stationary solution for the velocity component in the flow direction on a quadratic cross section in an infinitely long pipe and for a constant pressure gradient. Therefore, the simulated $v^{\mathrm{BGK}}(\boldsymbol{\ell}, t)$ and $\rho^{\mathrm{BGK}}(\boldsymbol{\ell}, t)$ are inspected for convergence at the end of the simulation $t = t_{\mathrm{end}}$ and the assumption of a constant pressure gradient is checked. We define

$$\delta w(t, \mathrm{d}t) = \max_{\boldsymbol{\ell}\in(\mathcal{S}\cap\mathcal{P})}\left(\frac{w(\boldsymbol{\ell}, t) - w(\boldsymbol{\ell}, t - \mathrm{d}t)}{w(\boldsymbol{\ell}, t)}\right), \tag{33}$$

as the maximum relative change of a quantity w during the time $\mathrm{d}t$ and within the computational domain $\mathcal{S}\cap\mathcal{P}$, where $w(\boldsymbol{\ell}, t)$ is either the velocity $v^{\mathrm{BGK}}(\boldsymbol{\ell}, t)$ or the density $\rho^{\mathrm{BGK}}(\boldsymbol{\ell}, t)$. Because the pressure is proportional to the density, equation (6), the pressure is converged if the density is sufficiently converged. The results from equation (33) are shown in table 1. In the simulations the velocities are of order $\hat{v}^{\mathrm{BGK}}(\boldsymbol{\ell}, t) \approx 10^{-4}$ so the absolute changes are of order 10^{-12}, using the relative changes δv from table 1. The fluid density is $\hat{\rho}^{\mathrm{BGK}}(\boldsymbol{\ell}, t) \approx 1.0$ giving absolute changes of order 10^{-5}. The variation of the

J. Stat. Mech. (2010) P11026

Table 1. Maximum relative change of the velocity $\delta v(t_{\rm end}, {\rm d}t)$ and density $\delta\rho(t_{\rm end}, {\rm d}t)$, equation (33), during the time ${\rm d}t$ when the simulation ended at $t_{\rm end}$. $\hat{B}$ is the dimensionless channel width.

$\hat{B}$	${\rm d}t/\Delta t$ $(\times 10^3)$	$t_{\rm end}/\Delta t$ $(\times 10^3)$	$\delta v(t_{\rm end}, {\rm d}t)$ $(\times 10^{-8})$	$\delta\rho(t_{\rm end}, {\rm d}t)$ $(\times 10^{-4})$
4	1	20	2.34	0.174
8	1	20	2.80	0.174
16	5	30	4.27	0.869
32	5	50	7.45	0.869
64	10	120	1.33	1.74

pressure gradient can be approximated by $2\,\delta\rho/(L_3) < 10^{-7}$. When calculating errors by comparing them with analytical solutions the number of significant digits is determined by the convergence of the simulation. We use the notation $v^{\rm BGK}(\boldsymbol{\ell})$, $\rho^{\rm BGK}(\boldsymbol{\ell})$ and $p^{\rm BGK}(\boldsymbol{\ell})$ for the velocity, density and pressure at the end of the simulation $t = t_{\rm end}$.

Due to the way we drive the flow, the pressure increases in the acceleration zone $\mathcal{F}$ and then decreases along the flow direction. See figure 8, where the average density $\langle\hat{\rho}\rangle_{\mathcal{C}(\ell_3)\cap\mathcal{P}} - 1$, from an LB-BGK simulation for a pipe of width $\hat{B} = 7$, is shown. To verify that the pressure gradient $(\nabla p)_3$ can be assumed to be constant as required by equation (30), we linearly fit $\langle p^{\rm BGK}\rangle_{\mathcal{C}(\ell_3)\cap\mathcal{P}}$ inside the sample. In the LB simulations, for pipes of width $\hat{B} = 4$, 8, 16, 32 and 64, all residues of the linear fit are of the order of 10^{-9}, so that the pressure gradient can be assumed to be constant.

Next, the velocity component in the flow direction $v^{\rm LB}(\boldsymbol{\ell})$ with $\boldsymbol{\ell} \in \mathcal{C}(L_3/2)$ is compared to the analytical solution equation (30), evaluated at the node positions $v^{\rm TH}(\mathbf{g}(\boldsymbol{\ell})_1, \mathbf{g}(\boldsymbol{\ell})_2)$. The cross section $\mathcal{C}(L_3/2)$ is chosen to minimize finite size effects and artifacts from the in/outlet chamber. We define absolute and relative errors of the velocities as

$$e_v^{\rm LB}(\boldsymbol{\ell}) := v^{\rm LB}(\boldsymbol{\ell}) - v^{\rm TH}(\mathbf{g}(\boldsymbol{\ell})_1, \mathbf{g}(\boldsymbol{\ell})_2), \tag{34}$$

$$\epsilon_v^{\rm LB}(\boldsymbol{\ell}) := \frac{v^{\rm LB}(\boldsymbol{\ell}) - v^{\rm TH}(\mathbf{g}(\boldsymbol{\ell})_1, \mathbf{g}(\boldsymbol{\ell})_2)}{v^{\rm TH}(\mathbf{g}(\boldsymbol{\ell})_1, \mathbf{g}(\boldsymbol{\ell})_2)}. \tag{35}$$

Figure 2 provides an overview on the structure of $|\epsilon_v^{\rm BGK}(\boldsymbol{\ell})|$ and figure 3 shows $|\epsilon_v^{\rm BGK}(\boldsymbol{\ell})|$ with $\ell_2 = L_2/2$ and $\ell_3 = L_3/2$ as a log–linear plot for different pipes of width $\hat{B}$ and LB-BGK. The largest relative errors are located in the corners and close to the wall. As the resolution increases the relative error declines rapidly. In the central region it is much smaller than 1%. To gain insight into how strong the value of the relaxation time τ influences the accuracy of the velocity field, simulations with LB-BGK and LB-MRT and different relaxation times $\hat{\tau} = 0.7$, 1.0, 2.0, 2.5 and 3.0 are investigated. Figure 4 displays the relative error of the velocity $\epsilon_v^{\rm LB}(\boldsymbol{\ell})$, equation (35), with $\ell_2 = \hat{B}/2$, $\ell_3 = L_3/2$ and $\hat{B} = 20$ for both implementations LB-BGK and LB-MRT and different relaxation times. The calculated velocity in the center of the pipe is in good agreement with the theoretical solution, having a relative error smaller than 1%. It is interesting to note that, when using the LB-BGK method, the largest error occurs for a large relaxation time $\hat{\tau} = 3.0$ (over-relaxation), whereas the largest error for the LB-MRT result occurs at a

J. Stat. Mech. (2010) P11026

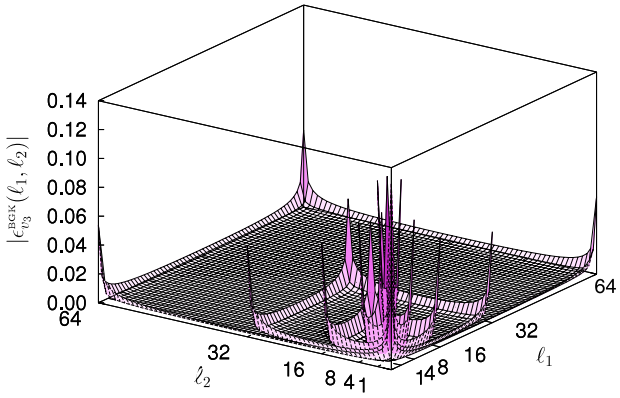

Figure 2. Overview of the relative error $|\epsilon_v^{\mathrm{BGK}}(\boldsymbol{\ell})|$ with $\ell_3 = L_3/2$, for pipes of widths $\hat{B} \in \{4, 8, 16, 32, 64\}$. Nodes at the corners cause the largest error followed by those close to the solid walls. For larger pipes the error decreases substantially.

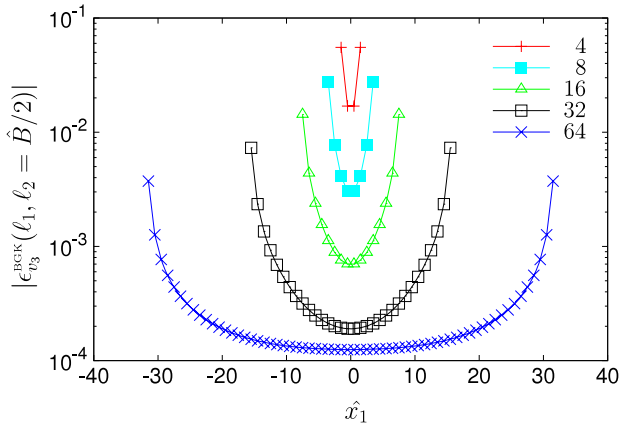

Figure 3. Log–linear plot of the relative error along the central line on a cross section, i.e. $|\epsilon_v^{\mathrm{BGK}}(\boldsymbol{\ell})|$ with $\ell_2 = L_2/2$ and $\ell_3 = L_3/2$. The error is largest at the walls and declines towards the center of the pipe. Different line styles indicate different pipe widths $\hat{B} = 4, 8, 16, 32$ and 64 as shown in the legend.

small relaxation time $\hat{\tau} = 0.7$ (under-relaxation). The calculated velocities tend to be overestimated $\epsilon_v^{\mathrm{BGK}}(\boldsymbol{\ell}) > 0$ for LB-BGK simulations and underestimated $\epsilon_v^{\mathrm{MRT}}(\boldsymbol{\ell}) < 0$ for LB-MRT simulations. When using LB-MRT the relative error is smaller by roughly a factor 10^{-2} when compared to results of the LB-BGK method.

For permeability calculations from Darcy's law, see equation (36), the mean velocity $\langle v^{\mathrm{LB}} \rangle_{\mathcal{S}}$ is used. Therefore, the mean relative error $\langle |\epsilon_v^{\mathrm{BGK}}| \rangle_{\mathcal{S}}$ and the mean absolute error $\langle |e_v^{\mathrm{BGK}}| \rangle_{\mathcal{S}}$ are of interest. Both decrease when $\hat{B}$ increases, as shown in table 2. The mean relative error shows a power law behavior $\langle |\epsilon_v^{\mathrm{BGK}}| \rangle_{\mathcal{S}} = a_1 \hat{B}^{a_2}$, with parameters $a_1 \approx 0.6$ and $a_2 \approx -1.6$. This relation can be used to calculate the relative error for arbitrary pipe widths B. Overall, the LB-BGK implementation is able to reproduce the velocity field for quadratic pipes very accurately. The mean relative error $\langle |\epsilon_v^{\mathrm{BGK}}| \rangle_{\mathcal{S}}$ is below 1% if the pipes are resolved better than $\hat{B} > 14$.

J. Stat. Mech. (2010) P11026

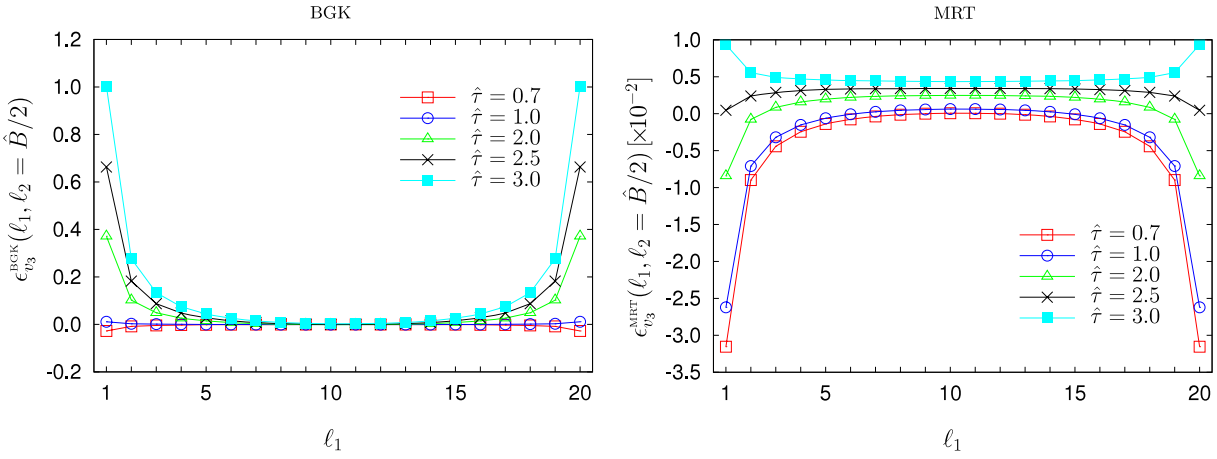

Figure 4. Relative error $\epsilon_v^{\mathrm{LB}}(\boldsymbol{\ell})$ with $\ell_2 = \hat{B}/2$ and $\ell_3 = L_3/2$ for flow in a quadratic pipe of width $\hat{B} = 20$ and different values of $\hat{\tau}$. The upper figure shows the results for the BGK implementation and in the lower figure the MRT results are shown. The relative error of the MRT simulations is smaller by 10^{-2} than the BGK results.

Table 2. Mean relative error $\langle|\epsilon_v^{\mathrm{BGK}}|\rangle_{\mathcal{S}}$ and absolute error $\langle|\hat{\epsilon}_v^{\mathrm{BGK}}|\rangle_{\mathcal{S}}$ for different pipes with width $\hat{B}$. The error declines rapidly as the pipe width increases.

$\hat{B}$	$\langle\lvert\epsilon_v^{\mathrm{BGK}}\rvert\rangle_{\mathcal{S}}$	$\langle\lvert\hat{\epsilon}_v^{\mathrm{BGK}}\rvert\rangle_{\mathcal{S}}$ $(\times 10^{-6})$
4	0.064099	0.300
8	0.021840	0.114
16	0.007241	0.068
32	0.002331	0.034
64	0.000784	0.023

Following the evaluation of the calculated velocity field, permeabilities are calculated using both implementations LB-BGK and LB-MRT. The permeability κ^{LB} is calculated using Darcy's law:

$$\kappa^{\mathrm{LB}} = -\eta \frac{\langle v^{\mathrm{LB}} \rangle_{\mathcal{S}}}{\langle (\nabla p)_3^{\mathrm{LB}} \rangle_{\mathcal{S}}}, \tag{36}$$

where η is the dynamic viscosity, $\langle v_3^{\mathrm{LB}} \rangle_{\mathcal{S}}$ is the average velocity in the sample and $\langle (\nabla p)_3^{\mathrm{LB}} \rangle_{\mathcal{S}}$ is the average pressure gradient component in the direction of flow. Details of how $\langle (\nabla p)_3^{\mathrm{LB}} \rangle_{\mathcal{S}}$ can be determined from $\rho^{\mathrm{LB}}(\boldsymbol{\ell})$ will be discussed later in this paper. The dynamic viscosity is calculated as $\eta = \nu \bar{\rho}^{\mathrm{LB}}$ with $\bar{\rho}^{\mathrm{LB}} = \langle \rho^{\mathrm{LB}} \rangle_{\mathcal{P} \cap \mathcal{S}}$ approximated by

$$\bar{\rho}^{\mathrm{LB}} \approx \frac{\langle \rho^{\mathrm{LB}} \rangle_{\mathcal{C}(L_{\mathcal{I}}+1)} + \langle \rho^{\mathrm{LB}} \rangle_{\mathcal{C}(L_3 - L_{\mathcal{O}})}}{2}. \tag{37}$$

The analytically obtained permeability is [44]

$$\kappa^{\mathrm{TH}}(B) = \lim_{M \to \infty} \frac{B^2}{4} \left(\frac{1}{3} - \frac{64}{\pi^5} \sum_{n=0}^{M} \frac{\tanh\left((2n+1)(\pi/2)\right)}{(2n+1)^5} \right), \tag{38}$$

J. Stat. Mech. (2010) P11026

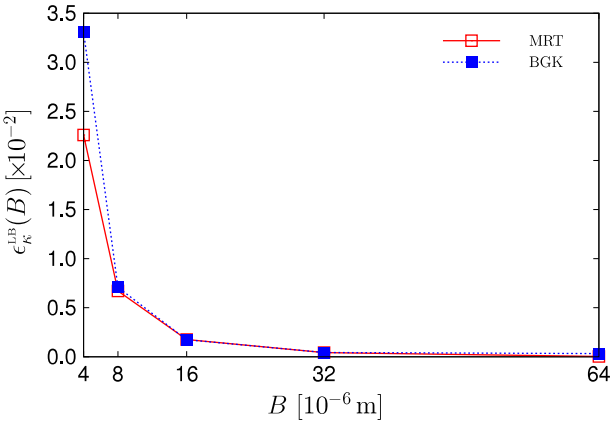

Figure 5. Relative error, $\epsilon_\kappa(B)$, of the permeability $\kappa^{\mathrm{LB}}(B)$ versus channel width B at fixed resolution $\Delta x = 10^{-6}$ m as calculated using LB-BGK (solid line) and LB-MRT (dashed line) simulations.

where we use $M = 200$ for numerical evaluation. To evaluate the error we define

$$\epsilon_\kappa^{\mathrm{LB}}(B) := \frac{\kappa^{\mathrm{LB}}(B) - \kappa^{\mathrm{TH}}(B)}{\kappa^{\mathrm{TH}}(B)}. \tag{39}$$

The relative errors $\epsilon_\kappa^{\mathrm{BGK}}(B)$ and $\epsilon_\kappa^{\mathrm{MRT}}(B)$ are shown in figure 5 and it can be observed that they fall below 1% for all pipes wider than $B = 16\Delta x$. It seems that the LB-BGK method is slightly more accurate, but the relaxation time $\hat{\tau} = 0.857$ was fine-tuned to reproduce the exact result with LB-BGK. Figure 5 shows that an adjusted relaxation parameter $\hat{\tau}$ can make up for the methodically inferior LB-BGK implementation. In realistic porous media, however, it is not possible to determine an optimal relaxation time τ, because the pore diameters and pore throats vary, although a useful range of τ can be determined, see section 5. Therefore the LB-MRT method is more reliable as its results are less dependent on τ.

The results for the velocity field and permeability show that even for a simple quadratic channel a resolution of at least 20 lattice nodes is required to achieve an accuracy of the permeability of order 1%. At present, discretization at this resolution is neither experimentally available nor computationally manageable.

5. Potential difficulties leading to inaccuracies

In this section we discuss typical difficulties arising when calculating permeabilities for complex geometries. This includes the influence of the relaxation time τ on the permeability, the accurate approximation of the average pressure gradient, the implementation of the external force and the discretization error.

When using SBB, the relaxation time τ slightly changes the position of the boundary between adjoined fluid–solid nodes. Due to this effect the relaxation time has a substantial influence on the permeability calculation [33]. One also has to be aware that this effect is always correlated with the discretization error and cannot be corrected analytically when investigating stochastic porous media. To analyze the influence of τ on the permeability

J. Stat. Mech. (2010) P11026

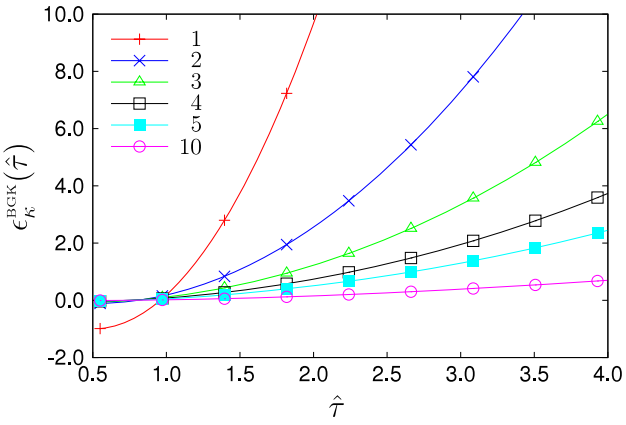

Figure 6. Relative error $\epsilon_\kappa^{\mathrm{LB}}$ versus the value of $\hat{\tau}$ for a Poiseuille flow in a quadratic pipe with different pipe width $\hat{B} = 1, 2, 3, 4, 5$ and 10 as indicated by different line styles.

we again investigate Poiseuille flow in quadratic pipes using a computational grid aligned with the pipe geometry to minimize the discretization error. The relative error $\epsilon_\kappa^{\mathrm{LB}}(\hat{\tau})$ is shown in figures 6 and 7. For over-relaxed systems ($\hat{\tau} > 1$), the LB-BGK method yields incorrect results, increasing dramatically the dependence of permeability on τ when the geometry is poorly discretized ($\hat{B} \leq 5$). If $\hat{\tau} \in [0.5, 1.0]$, the absolute error of permeability estimation is less than 3% for all $\hat{B} > 2$. The LB-MRT method has to be considered more reliably in general because the influence of τ is much smaller and the influence of τ_{bulk} is practically insignificant. For example, in figure 7, using a value $\hat{\tau} = 3.5$, the error of the LB-BGK method is 53.70%, while the error of the LB-MRT method is 4.213%. However, if only a small number of nodes is used ($\hat{B} \geq 5$) even the LB-MRT method produces a substantial error. Figure 7 compares the results between the LB-BGK and LB-MRT for a pipe with $\hat{B} = 10$. Here, both absolute errors in the interval $\hat{\tau} \in [0.5, 1.0]$ are smaller than 1.5%. It is important to stress here that outside the interval $\hat{\tau} \in [0.5, 1.0]$ the LB-MRT results remain accurate when B decreases, which is not the case for LB-BGK.

To compute the permeability using Darcy's law as given in equation (36), the average pressure gradient in the direction of flow $\langle(\nabla p)_3\rangle_{\mathcal{S}}$ is required. Because the permeability can strongly depend on the way the pressure gradient is obtained, alternative methods for its determination are discussed:

(a) Calculating the slope of a linear fit through the full dataset $\langle p\rangle_{\mathcal{C}(\ell_3)\cap\mathcal{P}}$ obtained using all cross sections $\mathcal{C}(\ell_3)$, $L_{\mathcal{I}} + 1 \leq \ell_3 \leq L_3 - L_{\mathcal{O}}$.

(b) As (a), but using only the cross sections $\mathcal{C}(\ell_3)$, $L_{\mathcal{I}} + 1 + W \leq \ell_3 \leq L_3 - L_{\mathcal{O}} - W$, $W \in \mathbb{N}$, see figure 8. The cross sections closer than W to the inlet and outlet of the sample are not taken into account. The idea is to minimize boundary effects.

(c) Approximation of $\langle(\nabla p)_3\rangle_{\mathcal{S}}$ by the arithmetic mean of the pressure at $\mathcal{C}(L_{\mathcal{I}} + 1)$ and $\mathcal{C}(L_3 - L_{\mathcal{O}})$, i.e.

$$\langle(\nabla p)_3\rangle_{\mathcal{S}} \approx \frac{\langle p\rangle_{\mathcal{C}(L_3 - L_{\mathcal{O}})\cap\mathcal{P}} - \langle p\rangle_{\mathcal{C}(L_{\mathcal{I}}+1)\cap\mathcal{P}}}{(L_{\mathcal{S}} - 1)\Delta x}, \tag{40}$$

where $L_{\mathcal{S}}$ is the sample length.

J. Stat. Mech. (2010) P11026

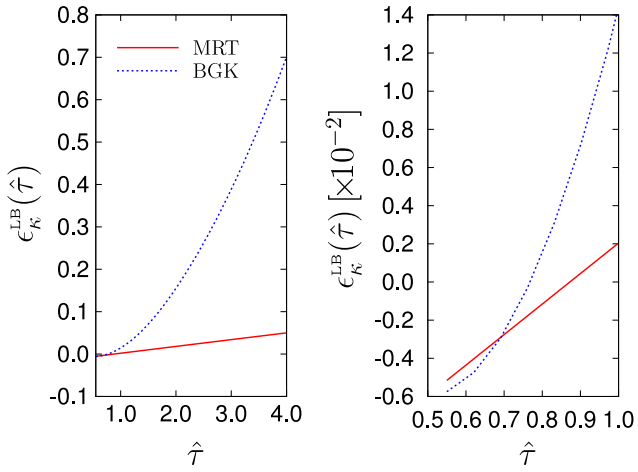

Figure 7. Relative error $\epsilon_\kappa^{\mathrm{LB}}$ for Poiseuille flow in a quadratic pipe with width $\hat{B} = 10$, calculated using LB-BGK, dashed line, and LB-MRT, solid line. On the left, the interval $\hat{\tau} \in [0.5, 4.0]$ is shown and on the right, a zoom in the interval $\hat{\tau} \in [0.5, 1.0]$ can be seen.

(d) Approximation of $\langle(\nabla p)_3\rangle_{\mathcal{S}}$ by the arithmetic mean of the pressure at $\mathcal{C}(L_{\mathcal{I}})$ and $\mathcal{C}(L_3 - L_{\mathcal{O}} + 1)$, i.e.

$$\langle(\nabla p)_3\rangle_{\mathcal{S}} \approx \frac{\langle p\rangle_{\mathcal{C}(L_3 - L_{\mathcal{O}}+1)\cap\mathcal{P}} - \langle p\rangle_{\mathcal{C}(L_{\mathcal{I}})\cap\mathcal{P}}}{(L_{\mathcal{S}} + 1)\Delta x}. \tag{41}$$

For a quantitative comparison of the different methods simulations with the following parameters are performed:

$$\begin{aligned}
&L_1 = 40,\ L_2 = 40,\ L_3 = 80,\\
&\mathcal{S} = \{\boldsymbol{\ell} \in \mathcal{L} : 17 \le \ell_1 \le 23, 17 \le \ell_2 \le 23, 21 \le \ell_3 \le 60\},\\
&\mathcal{I} = \{\boldsymbol{\ell} \in \mathcal{L} : 1 \le \ell_3 \le 20\}, \mathcal{O} = \{\boldsymbol{\ell} \in \mathcal{L} : 61 \le \ell_3 \le 80\},\\
&\mathcal{F} = \{\boldsymbol{\ell} \in \mathcal{L} : 6 \le \ell_3 \le 15\}, L_{\mathcal{I}} = 20, L_{\mathcal{S}} = 40, L_{\mathcal{O}} = 20.
\end{aligned}$$

The average density $\langle\hat{\rho}\rangle_{\mathcal{C}(\ell_3)\cap\mathcal{P}}$ is shown in figure 8. Although the density field $\rho(\boldsymbol{\ell})$ is continuous, the average $\langle\rho\rangle_{\mathcal{C}(\ell_3)\cap\mathcal{P}}$ shows two discontinuities, one at the beginning of the sample ($\ell_3 = 20$) and one at the end of the sample ($\ell_3 = 60$). These can be explained by the small compressibility of the fluid. The majority of the fluid in chamber $\mathcal{I}$ flows towards the surface of the sample causing an increased local density. The same effect can be observed right behind the sample where one finds a low density due to the fluid compressibility. Because we use periodic boundary conditions, the pressure is almost constant in both chambers $\mathcal{I}$ and $\mathcal{O}$ and only increases in the acceleration zone $\mathcal{F}$. The small increment right before the sample and the small decrement right after the sample are both imperceptible in figure 8. The results presented in table 3 show that, by using alternatives (a), (b) and (c), an error smaller than 1% can be obtained. The remaining method (d), however, shows a substantially larger error and is therefore not suitable for measuring the pressure gradient. Alternative (b) is not taking into account the cross sections closer than $W = 10$ to the inlet and outlet of the sample. Changing W does not

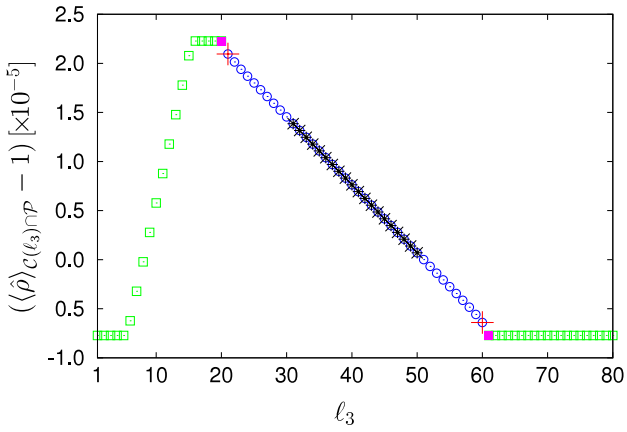

Figure 8. Average density $(\langle\hat{\rho}\rangle_{\mathcal{C}(\ell_3)\cap\mathcal{P}} - 1)$ versus ℓ_3 as obtained from an LB-BGK simulation. The sample $\mathcal{S}$ is placed in $\ell_3 \in [21, 60]$, leaving 20 nodes before and after the sample as the injection chamber. Within the acceleration zone $\mathcal{F}$ at $\ell_3 \in [6, 15]$ the density and pressure increase. Alternatives to measuring the density or pressure gradient: (a) use all nodes inside the sample for a linear fit ($\odot$). (b) Linear fit not using the nodes closer than $W = 10$ to the point where the fluid enters or leaves the sample ($\times$). (c) Use the first and last cross section $\mathcal{C}(L_\mathcal{I}+1)$ and $\mathcal{C}(L_3-L_\mathcal{O})$ inside the sample ($+$). (d) Use the cross sections $\mathcal{C}(L_\mathcal{I})$ and $\mathcal{C}(L_3-L_\mathcal{O}+1)$ ($\blacksquare$). The nodes represented by $\square$ define the injection channel ($\mathcal{I}$ and $\mathcal{O}$).

Table 3. Results of the three alternatives to measure $\langle(\nabla p)_3\rangle_\mathcal{S}$ and the case without using an injection channel. Shown are calculated permeabilities and their relative error for $\hat{B} = 7$. For alternative (b) $W = 10$ is used.

$\hat{B} = 7$	(a)	(b)	(c)	(d)
$\hat{\kappa}^{\mathrm{LB}}$	1.732 44	1.736 89	1.713 46	1.642 70
ϵ_κ (%)	0.614 23	0.872 78	0.487 87	4.597 61
Without injection channel				
$\hat{\kappa}^{\mathrm{LB}}$	1.736 89			
ϵ_κ (%)	0.872 77			

influence the accuracy much. For stochastic porous media we suggest using alternative (c) because it is very easy to implement and no fit is necessary. The last row of table 3 shows the values obtained without an injection chamber and with a force acting throughout the whole domain. Even though the result is accurate, this method has a major disadvantage, because it can only be applied to periodic samples and not to stochastic porous media. In realistic porous media, chambers before and after the sample are necessary to provide a fluid reservoir but they might decrease the accuracy of the method due to disturbances of the velocity field at the in- and outlet.

An important point for performing high precision permeability measurements is the way the pressure gradient is generated. While pressure boundary conditions provide a well-defined way of fixing the pressure at the in- and outlet, they assume an ideal gas and

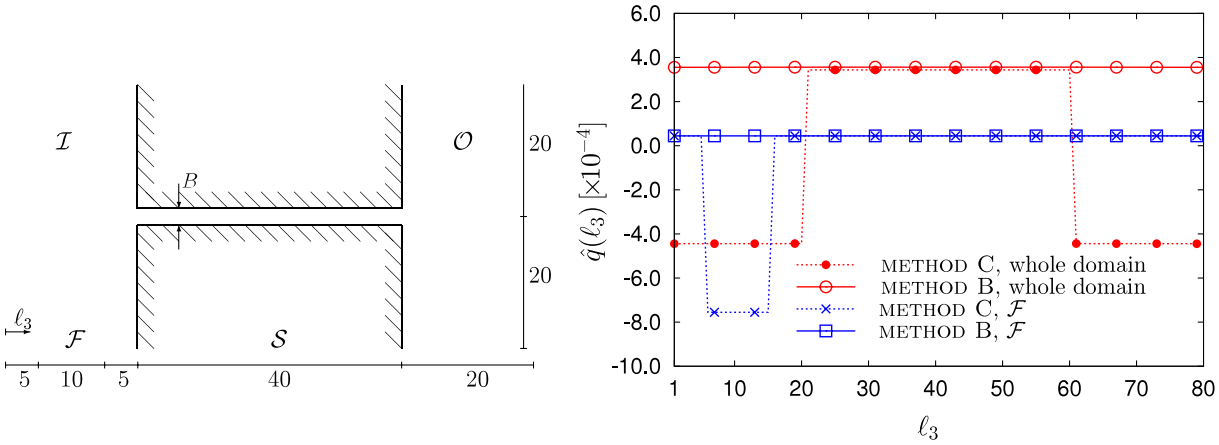

Figure 9. Mass flux $q(\ell_3)$ in a quadratic pipe of width $\hat{B} = 5$ as obtained from an LB-BGK simulation. If the acceleration is implemented as defined by METHOD C, $q(\ell_3)$ is not constant in the regions where the acceleration is applied. METHOD B ensures a correct constant mass flux $q(\ell_3)$ throughout the whole domain.

are slightly harder to implement than a simple body force driving the flow. In addition, even though the pressure is fixed before and after the sample, an injection chamber is still required and for high precision permeability measurements one has to measure the pressure gradient as discussed above. Therefore, most LB implementations found in the literature use body forces. In fact, all papers we are aware of, that have been published before 2002, and a large fraction of more recent publications use an incorrect force implementation which can lead to severely erroneous permeabilities. Popular examples for such implementations are METHOD C and METHOD D. They lead to an underestimation of the velocity $\mathbf{v}(\boldsymbol{\ell})$ in the direction of the flow on the lattice nodes where the acceleration is acting. Many publications apply the force throughout the whole simulation domain. The results obtained from such implementations cannot be trusted for two reasons: firstly, in METHOD C and METHOD D the macroscopic velocity in the acceleration zone is smaller than the correct value. In some cases it can even be negative. Secondly, the pore structure plays an important role. The number of nodes at any cross section $\mathcal{C}(\ell_3)$ determines the number of times the additional acceleration term has to be added to the mass flow in order to ensure a constant flux.

In figure 9 we compare METHOD B and METHOD C. All simulation parameters except the pipe width ($\hat{B} = 5$) are kept as before so that

$$\mathcal{S} = \{\boldsymbol{\ell} \in \mathcal{L} : 18 \leq \ell_1 \leq 22, 18 \leq \ell_2 \leq 22, 21 \leq \ell_3 \leq 60\}. \tag{42}$$

The line representing the application of METHOD C and the external acceleration applied throughout the whole domain has discontinuities exactly at the position where the width of the channel changes abruptly, i.e. at $\ell_3 = 20$ and 60 (local porosity dependence). The line representing the application of METHOD C throughout an acceleration zone $\mathcal{F}$ shows discontinuities within the acceleration zone, i.e. in the interval $\ell_3 \in [6, 15]$. These discontinuities are not present when using METHOD B. The term $\eta\langle v_3\rangle_s$ in Darcy's law (see equation (36)) is usually approximated by $Q\nu/A$, where the total mass flux Q is calculated by averaging $q(\ell_3)$ in the whole sample. A represents the sample cross-sectional area.

J. Stat. Mech. (2010) P11026

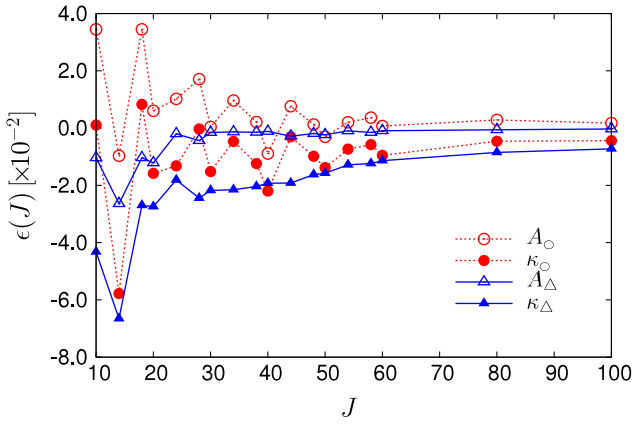

Figure 10. Relative errors in the area discretization $\epsilon_A^{\mathrm{BGK}}$ and permeability estimation $\epsilon_\kappa^{\mathrm{BGK}}$ for a circular and triangular cross-section pipe with different system sizes J. The permeability error correlates with the discretization error. Compared to the results for quadratic pipes, the permeability error is, at the same resolution, approximately twice as large.

If an external acceleration is not implemented correctly, the calculated Q is always incorrect, leading to a wrong estimate of κ. For the example in figure 9 which uses METHOD C and a force throughout the whole domain, Q is underestimated but remains positive. This is not the case if an acceleration zone $\mathcal{F}$ is used. Here, the calculation of Q leads to an unphysical negative result, so that the permeability is always underestimated and in some cases negative. Such cases can also be observed for inhomogeneous stochastic porous media, where the variation of pore sizes is very large [45].

Another important issue is the effect of discretization. When investigating square pipes the lattice is aligned with the solid–fluid interface. This is not the case for the simulation of flow in realistic stochastic porous media. Thus, the influence of discretization effects is substantially larger than in the ideal cases presented before. We investigate the order of the resulting error by calculating the permeabilities in pipes with a circular and an equilateral triangular cross section. The samples are of size $L_1 = J$, $L_2 = J$ and $L_3 = 4J$ with $J \in \mathbb{N}$ and the cross sections are defined by their diameter $B_\bigcirc$ (circular) or their side length $B_\triangle$ (equilateral triangle) with $B_\bigcirc = B_\triangle = (J-2)\Delta x$. The analytical solutions for the permeabilities of circular and equilateral triangular pipes are

$$\kappa_\bigcirc^{\mathrm{TH}} = \frac{A_\bigcirc^{\mathrm{TH}}}{8\pi}, \qquad A_\bigcirc^{\mathrm{TH}} = \frac{\pi}{4} {B_\bigcirc}^2, \tag{43}$$

$$\kappa_\triangle^{\mathrm{TH}} = \frac{\sqrt{3} A_\triangle^{\mathrm{TH}}}{60}, \qquad A_\triangle^{\mathrm{TH}} = \frac{\sqrt{3}}{4} {B_\triangle}^2, \tag{44}$$

where $A_\bigcirc^{\mathrm{TH}}$ and $A_\triangle^{\mathrm{TH}}$ are the cross-sectional areas. Discretizing these areas on a cubic lattice results in approximate cross-sectional areas $A_\triangle^{\mathrm{LB}}$ and $A_\bigcirc^{\mathrm{LB}}$. Let $\epsilon_{A_\triangle}^{\mathrm{LB}}$ and $\epsilon_{A_\bigcirc}^{\mathrm{LB}}$ be the relative discretization errors of those areas. The permeabilities as calculated from the simulation results are $\kappa_\triangle^{\mathrm{BGK}}$ and $\kappa_\bigcirc^{\mathrm{BGK}}$, with their relative errors being $\epsilon_{\kappa_\triangle}^{\mathrm{BGK}}$ and $\epsilon_{\kappa_\bigcirc}^{\mathrm{BGK}}$. Figure 10 depicts that for both geometries the relative error of the permeabilities is much larger than for pipes with quadratic cross section, see figure 5 for comparison.

J. Stat. Mech. (2010) P11026

Furthermore, it can be seen that the error in permeability correlates with the error of the discretized area. This discretization error is not present when investigating square pipes that are aligned with the grid. In stochastic porous media this discretization error is inevitable. Therefore, arbitrarily structured pore throats have to be resolved at a much higher resolution for high precision permeability calculations. This is a serious limitation when calculating permeabilities for laboratory sized porous media using the techniques discussed in this paper.

6. Application to Fontainebleau sandstones

After validating the simulation results, determining errors for pipe flow and pointing out problems when calculating permeabilities with LB implementations, we now apply our findings to investigate a porous sample. We calculate the permeability of a sample of Fontainebleau sandstone, gained by thresholding a discretized μ-CT dataset. This particular data is chosen because it has been investigated previously using a finite difference method and another LB implementation [12]. The results for the calculated permeabilities in [12] show excellent agreement with the experimental results in [46]. Therefore this sample serves as a benchmark for the permeability calculations presented here. Calculations are carried out at a low (l.r.) and high resolution (h.r.). The l.r. computational domain is

$$
\begin{aligned}
&L_1 = 305,\ L_2 = 305,\ L_3 = 320,\\
&\mathcal{S} = \{\boldsymbol{\ell} \in \mathcal{L} : 3 \le \ell_1 \le 303, 3 \le \ell_2 \le 303, 11 \le \ell_3 \le 310\},\\
&\mathcal{I} = \{\boldsymbol{\ell} \in \mathcal{L} : 1 \le \ell_3 \le 10\}, \mathcal{O} = \{\boldsymbol{\ell} \in \mathcal{L} : 311 \le \ell_3 \le 320\},\\
&\mathcal{F} = \{\boldsymbol{\ell} \in \mathcal{L} : 1 \le \ell_3 \le 5\}, L_{\mathcal{I}} = 10,\ L_{\mathcal{S}} = 300,\ L_{\mathcal{O}} = 10,\\
&\Delta x = 7.5 \times 10^{-6}\ \text{m}.
\end{aligned}
$$

The high resolution sample is created from the low resolution sample by substituting every voxel with eight voxels on a cubic sublattice. The h.r. computational domain is

$$
\begin{aligned}
&L_1 = 605,\ L_2 = 605,\ L_3 = 620,\\
&\mathcal{S} = \{\boldsymbol{\ell} \in \mathcal{L} : 3 \le \ell_1 \le 602, 3 \le \ell_2 \le 602, 11 \le \ell_3 \le 610\},\\
&\mathcal{I} = \{\boldsymbol{\ell} \in \mathcal{L} : 1 \le \ell_3 \le 10\}, \mathcal{O} = \{\boldsymbol{\ell} \in \mathcal{L} : 611 \le \ell_3 \le 620\},\\
&\mathcal{F} = \{\boldsymbol{\ell} \in \mathcal{L} : 1 \le \ell_3 \le 5\}, L_{\mathcal{I}} = 10,\ L_{\mathcal{S}} = 600,\ L_{\mathcal{O}} = 10,\\
&\Delta x = 3.75 \times 10^{-6}\ \text{m}.
\end{aligned}
$$

For the permeability calculation an approximation of Darcy's law is used, see equations (36), (40) and (37):

$$
\kappa = -\frac{\nu(L_{\mathcal{S}} - 1)\Delta x \,\langle v_3\rangle_{\mathcal{S}}(\langle\rho\rangle_{\mathcal{C}(L_{\mathcal{I}}+1)\cap\mathcal{P}} + \langle\rho\rangle_{\mathcal{C}(L_3-L_{\mathcal{O}})\cap\mathcal{P}})}{2\,(\langle p\rangle_{\mathcal{C}(L_3-L_{\mathcal{O}})\cap\mathcal{P}} - \langle p\rangle_{\mathcal{C}(L_{\mathcal{I}}+1)\cap\mathcal{P}})}. \tag{45}
$$

The kinematic viscosity ν is calculated using equation (15) with $\hat{\tau}$, as in table 4, $\hat{\tau}_{\text{bulk}} = 1.0$ and Δt from equation (7) with $c_{\text{s}} = 1\ \text{m s}^{-1}$. Simulations are performed with the LB-BGK and LB-MRT method for 100 000 time steps. The relaxation times used in the simulation and the calculated permeabilities for the l.r. h.r. sample and from [12] are given in table 4. The calculated permeabilities $\kappa_{\text{l.r.}}$ and $\kappa_{\text{h.r.}}$ were linearly extrapolated for infinite resolution at $1/L_{\mathcal{S}} = 0$ yielding κ_{extrap}.

J. Stat. Mech. (2010) P11026

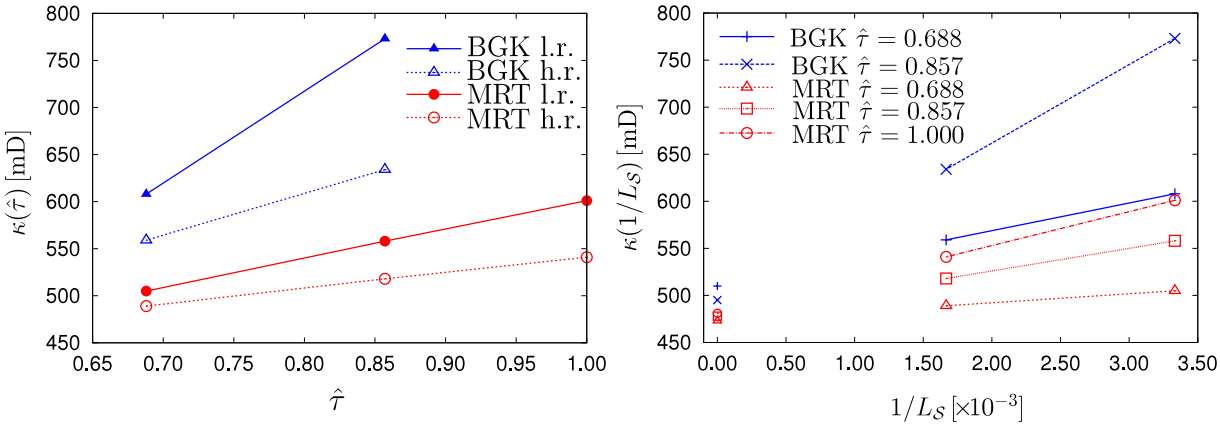

Figure 11. The top plot shows the permeability for different $\hat{\tau}$, LB schemes, the l.r. and the h.r. sample. The influence of $\hat{\tau}$ on the permeability is stronger using the BGK implementation. The bottom plot shows the permeability results, for the l.r. sample with $L_{\mathcal{S}} = 300$ and the h.r. sample with $L_{\mathcal{S}} = 600$. At $1/L_{\mathcal{S}} = 0$ the extrapolated permeabilities κ_{extrap} are shown.

Table 4. Simulation results of the permeability calculations for the Fontainebleau sandstone. Results for the low resolution sample are labeled $\kappa_{\text{l.r.}}$, the high resolution sample results $\kappa_{\text{h.r.}}$ and the extrapolation results κ_{extrap}. Different relaxation times $\hat{\tau}$ and LB-BGK and LB-MRT implementations are compared.

LB method	$\hat{\tau}$	$\kappa_{\text{l.r.}}$ (mD)	$\kappa_{\text{h.r.}}$ (mD)	κ_{extrap} (mD)
BGK [12]	0.688	621	—	—
BGK	0.688	608	559	510
BGK	0.857	773	634	495
MRT	0.688	505	489	473
MRT	0.857	558	518	478
MRT	1.000	601	541	481

Our result $\kappa_{\text{l.r.}} = 608$ (mD) for $\hat{\tau} = 0.688$, see table 4, is in good agreement with the result in [12] being $\kappa = 621$ (mD). Although the simulation set-up is different, a relative difference of only 2% is obtained. Figure 11 (top) confirms that permeability results gained from LB-BGK simulations are particularly dependent on the relaxation time $\hat{\tau}$ that is used. Therefore, when investigating complex geometries, where $\hat{\tau}$ cannot be optimized for a specific geometrical shape, a LB-MRT should be used. As expected, when calculating permeabilities for complex geometries, the influence of $\hat{\tau}$ is much stronger than within simple geometries, i.e. square pipes, see sections 4 and 5 together with figure 7. The extrapolated permeabilities κ_{extrap} are an estimate for the true permeability of the discretized μ-CT sample at resolution 3.75×10^{-6} m and not the true permeability of the sandstone. To estimate the true permeability of the sandstone by extrapolation, new μ-CT data with higher resolutions would be required. However, from figure 11 (bottom) it can be seen that the extrapolated permeability values have a small spread, in a range from 473 to 510 (mD), regardless of the simulation method and relaxation time used. This indicates that, if sufficiently high resolved sample data and computer performance are

J. Stat. Mech. (2010) P11026

available, an extrapolation analysis, even using LB-BGK $\hat{\tau} = 1$ results, might give a good approximation of the true permeability. One could expect that errors due to random geometries would experience random cancellations. However, the results presented in figure 11 clearly show that this is not true for a realistic porous medium.

7. Conclusion

Our simulation set-up of an acceleration zone and in/outlet chambers, together with our approximations of Darcy's law, provides a method for permeability calculations. Several problems in the numerical implementation and data evaluation were addressed, such as a correct acceleration implementation and an adequate approximation for calculating the pressure gradient. Caveats when using LB simulations to calculate permeabilities have been exposed. We performed detailed studies with different LB implementations, i.e. BGK and MRT, and for various systems to quantitatively determine the accuracy of the calculated velocity field and calculated permeability. We find that, for reasonably resolved quadratic pipes, the error of the calculated permeability is below 1%. Investigating non-aligned geometries, circular and triangular pipes, the discretization and permeability error is roughly 4% at comparable resolutions. From this we infer that permeability calculations in stochastic porous media will have a significantly larger error, because the resolution of pores and pore walls is usually well below the resolution used for our pipe calculations above. Comparing the two LB implementations, LB-BGK and LB-MRT, we find that LB-MRT reduces the dependence of the permeability on the value of τ substantially. Using LB-BGK and a relaxation time τ tailored to give good results for a specific geometry does not ensure reliable results in a stochastic porous medium. For example, we found that LB-BGK and $\hat{\tau} = 0.857$ yield the best result for 3D Poiseuille flow in a quadratic pipe. However, for this value LB-BGK and LB-MRT results differ by 20% if applied to the Fontainebleau sandstone (see figure 11). Therefore, LB-MRT is suggested to be used for permeability estimates based on LB simulations. Further investigations using the LB method for flow through stochastic porous media should include a resolution and relaxation time-dependent analysis together with an appropriate extrapolation scheme for more reliable permeability estimates.

Acknowledgments

We are grateful to the High Performance Computing Center in Stuttgart, the Scientific Supercomputing Center in Karlsruhe and the Jülich Supercomputing Center for providing access to their machines. One of us (TZ) would like to acknowledge partial support from the DFG program EXC310 (Simulationstechnik). We would like to thank Bibhu Biswal for fruitful discussions and the Sonderforschungsbereich 716, the DFG program 'Nano- and microfluidics' and the Deutscher Akademischer Austauschdienst (DAAD) for financial support.

References

[1] Hilfer R, *Transport and relaxation phenomena in porous media*, 1996 *Adv. Chem. Phys.* **XCII** 299
[2] Hilfer R, *Local-porosity theory for flow in porous media*, 1992 *Phys. Rev.* B **45** 7115
[3] Koponen A, Kataja M and Timonen J, *Permeability and effective porosity of porous media*, 1997 *Phys. Rev.* E **56** 3319

J. Stat. Mech. (2010) P11026

[4] Dixon K L and Nichol R L, *Permeability estimation from transient vadose zone pumping tests in shallow coastal-plain sediments*, 2005 *Environ. Geosci.* **12** 279
[5] Gee G W, Zhang F Z and Ward A L, *A modified vadose zone fluxmeter with solution collection capability*, 2003 *Vadose Zone J.* **2** 627
[6] Addiscott T M and Whitmore A P, *Simulation of solute leaching in soils of differing permeabilities*, 2007 *Soil Use Mngt.* **7** 94
[7] Garrido P, Concha F and Bürger R, *Settling velocities of particulate systems: 14. unified model of sedimentation, centrifugation and filtration of flocculated suspensions*, 2003 *Int. J. Mineral Process* **72** 57
[8] Ferréol B and Rothman D H, *Lattice-Boltzmann simulations of flow through Fontainebleau sandstone*, 1995 *Transp. Porous Media* **20** 3
[9] Cancelliere A, Chang C, Foti E, Rothman D H and Succi S, *The permeability of a random medium: comparison of simulation with theory*, 1990 *Phys. Fluids* **2** 2085
[10] Qian Y H, d'Humières D and Lallemand P, *Lattice BGK models for Navier–Stokes equation*, 1992 *Europhys. Lett.* **17** 479
[11] Martys N S and Garboczi E J, *Length scales relating the fluid permeability and electrical conductivity in random two-dimensional model porous media*, 1992 *Phys. Rev.* B **46** 6080
[12] Manwart C, Aaltosalmi U, Koponen A, Hilfer R and Timonen J, *Lattice-Boltzmann and finite-difference simulations for the permeability of three-dimensional porous media*, 2002 *Phys. Rev.* E **66** 016702
[13] Succi S, 2001 *The Lattice Boltzmann Equation for Fluid Dynamics and Beyond* (Oxford: Oxford University Press)
[14] Martys N S, Hagedorn J G, Goujon D and Devaney J E, *Large scale simulations of single and multi-component flow in porous media*, 1999 *Developments in X-Ray Tomography II, Proc. SPIE* vol 3772, pp 205–13
[15] Harting J, Venturoli M and Coveney P, *Large-scale grid-enabled lattice-Boltzmann simulations of complex fluid flow in porous media and under shear*, 2004 *Phil. Trans. R. Soc. Lond.* A **362** 1703
[16] Ahrenholz B, Tölke J and Krafczyk M, *Lattice Boltzmann simulations in reconstructed parametrized porous media*, 2006 *Int. J. Comput. Fluid Dyn.* **20** 369
[17] Koponen A, Kandhai D, Hellén E, Alava M, Hoekstra A, Kataja M, Niskanen K, Sloot P and Timonen J, *Permeability of three-dimensional random fiber webs*, 1998 *Phys. Rev. Lett.* **80** 716
[18] Biswal B, Øren P-E, Held R, Bakke S and Hilfer R, *Stochastic multiscale model for carbonate rocks*, 2007 *Phys. Rev.* E **75** 061303
[19] Peng G, Xi H, Duncan C and Chou S-H, *Lattice Boltzmann method on irregular meshes*, 1998 *Phys. Rev.* E **58** R4124
[20] Ubertini S, Bella G and Succi S, *Lattice Boltzmann method on unstructured grids: further developments*, 2003 *Phys. Rev.* E **68** 016701
[21] Qian Y H, *Fractional propagation and the elimination of staggered invariants in lattice-BGK models*, 1997 *Int. J. Mod. Phys.* C **8** 753
[22] Higuera F J, Succi S and Benzi R, *Lattice gas dynamics with enhanced collisions*, 1989 *Europhys. Lett.* **9** 345
[23] Ladd A J C and Verberg R, *Lattice-Boltzmann simulations of particle–fluid suspensions*, 2001 *J. Stat. Phys.* **104** 1197
[24] Chen S, Chen H, Martínez D and Matthaeus W H, *Lattice Boltzmann model for simulation of magnetohydrodynamics*, 1991 *Phys. Rev. Lett.* **67** 3776
[25] Bhatnagar P L, Gross E P and Krook M, *Model for collision processes in gases. I. Small amplitude processes in charged and neutral one-component systems*, 1954 *Phys. Rev.* **94** 511
[26] Hänel D, 2004 *Molekulare Gasdynamik: Einführung in Die Kinetische Theorie der Gase und Lattice-Boltzmann-Methoden* (Berlin: Springer)
[27] d'Humières D, Ginzburg I, Krafczyk M, Lallemand P and Luo L-S, *Multiple-relaxation-time lattice Boltzmann models in three dimensions*, 2002 *Phil. Trans. R. Soc. Lond.* A **360** 437
[28] Lallemand P and Luo L-S, *Theory of the lattice Boltzmann method: dispersion, dissipation, isotropy, Galilean invariance, and stability*, 2000 *Phys. Rev.* E **61** 6546
[29] Ginzburg I, Verhaeghe F and d'Humières D, *Two-relaxation-time lattice Boltzmann scheme: about parametrization, velocity, pressure and mixed boundary conditions*, 2008 *Commun. Comput. Phys.* **3** 427
[30] Ginzburg I, Verhaeghe F and d'Humières D, *Study of simple hydrodynamic solutions with the two-relaxation-times lattice Boltzmann scheme*, 2008 *Commun. Comput. Phys.* **3** 519
[31] Chapman S and Cowling T G, 1952 *The Mathematical Theory of Non-Uniform Gases* 2nd edn (Cambridge: Cambridge University Press)
[32] Wolf-Gladrow D A, 2005 *Lattice-Gas Cellular Automata and lattice Boltzmann Models* (Berlin: Springer)

J. Stat. Mech. (2010) P11026

[33] Pan C, Luo L-S and Miller C T, *An evaluation of lattice Boltzmann schemes for porous medium flow simulation*, 2006 *Comput. Fluids* **35** 898
[34] Lallemand P and Luo L-S, *Theory of the lattice Boltzmann method: acoustic and thermal properties in two and three dimensions*, 2003 *Phys. Rev.* E **68** 036706
[35] Guo Z, Zheng C and Shi B, *Discrete lattice effects on the forcing term in the lattice Boltzmann method*, 2002 *Phys. Rev.* E **65** 046308
[36] He X, Zou Q, Luo L-S and Dembo M, *Analytic solutions and analysis on non-slip boundary conditions for the lattice Boltzmann BGK model*, 1997 *J. Stat. Phys.* **87** 115
[37] Sukop M C and Thorne D T Jr, 2007 *Lattice Boltzmann Modeling, An Introduction for Geoscientists and Engineers* 2nd edn (Berlin: Springer)
[38] Ginzburg I and d'Humières D, *Local second-order boundary methods for lattice Boltzmann models*, 1996 *J. Stat. Phys.* **84** 927
[39] Lallemand P and Luo L-S, *Lattice Boltzmann method for moving boundaries*, 2003 *J. Comput. Phys.* **184** 406
[40] Bouzidi M, Firdaouss M and Lallemand P, *Momentum transfer of a Boltzmann-lattice fluid with boundaries*, 2001 *Phys. Fluids* **13** 3452
[41] Ginzburg I and d'Humières D, *Multireflection boundary conditions for lattice Boltzmann models*, 2003 *Phys. Rev.* E **68** 066614
[42] Zou Q and He X, *On pressure and velocity boundary conditions for the lattice Boltzmann BGK model*, 1997 *Phys. Fluids* **9** 1591
[43] Hecht M and Harting J, *Implementation of on-site velocity boundary conditions for D3Q19 lattice Boltzmann simulations*, 2010 *J. Stat. Mech.* P01018
[44] Wieghardt K, 1957 *Theoretische Strömungslehre* Göttinger Klassik
[45] Narváez A, Raischel F, Harting J and Hilfer R, 2010 in preparation
[46] Manwart C, *Geometrische modellierung und transporteigenschaften poröser medien*, 2001 *PhD Thesis* Fakultät Physik der Universit Stuttgart (Berlin: Logos)

J. Stat. Mech. (2010) P11026